

Article

Modification of Cu Oxide and Cu Nitride Films by Energetic Ion Impact

Noriaki Matsunami ^{1,*}, Masao Sataka ², Satoru Okayasu ² and Bun Tsuchiya ¹ ¹ Faculty of Science and Technology, Meijo University, Nagoya 468-8502, Japan; btsuchiya@meijo-u.ac.jp² Japan Atomic Energy Agency (JAEA), Tokai 319-1195, Japan; sataka@tac.tsukuba.ac.jp (M.S.); okayasu.satoru@jaea.go.jp (S.O.)

* Correspondence: atsu20matsu@gmail.com

Abstract: We have investigated lattice disordering of copper oxide (Cu₂O) and copper nitride (Cu₃N) films induced by high- and low-energy ion impact, knowing that the effects of electronic excitation and elastic collision play roles by these ions, respectively. For high-energy ion impact, degradation of X-ray diffraction (XRD) intensity per ion fluence or lattice disordering cross-section (Y_{XD}) fits to the power-law: $Y_{XD} = (B_{XD}S_e)^{N_{XD}}$, with S_e and B_{XD} being the electronic stopping power and a constant. For Cu₂O and Cu₃N, N_{XD} is obtained to be 2.42 and 1.75, and B_{XD} is 0.223 and 0.54 (keV/nm)⁻¹. It appears that for low-energy ion impact, Y_{XD} is nearly proportional to the nuclear stopping power (S_n). The efficiency of energy deposition, Y_{XD}/S_e , as well as Y_{sp}/S_e , is compared with Y_{XD}/S_n , as well as Y_{sp}/S_n . The efficiency ratio $R_{XD} = (Y_{XD}/S_e)/(Y_{XD}/S_n)$ is evaluated to be ~0.1 and ~0.2 at $S_e = 15$ keV/nm for Cu₂O and Cu₃N, meaning that the efficiency of electronic energy deposition is smaller than that of nuclear energy deposition. $R_{sp} = (Y_{sp}/S_e)/(Y_{sp}/S_n)$ is evaluated to be 0.46 for Cu₂O and 0.7 for Cu₃N at $S_e = 15$ keV/nm.

Keywords: lattice disordering; sputtering; electronic excitation; elastic collision; energy deposition efficiency



Citation: Matsunami, N.; Sataka, M.; Okayasu, S.; Tsuchiya, B. Modification of Cu Oxide and Cu Nitride Films by Energetic Ion Impact. *Quantum Beam Sci.* **2024**, *8*, 12. <https://doi.org/10.3390/qubs8020012>

Academic Editor: Hiro Amekura

Received: 29 January 2024

Revised: 8 March 2024

Accepted: 8 April 2024

Published: 10 April 2024



Copyright: © 2024 by the authors. Licensee MDPI, Basel, Switzerland. This article is an open access article distributed under the terms and conditions of the Creative Commons Attribution (CC BY) license (<https://creativecommons.org/licenses/by/4.0/>).

1. Introduction

It is known that electronic excitation under energetic-ion impact leads to modifications of solids such as electronic sputtering (erosion of solid materials induced by electronic energy deposition) and track formation. For example, electronic sputtering by mono-energetic ions (>0.1 MeV/u) has been observed in many non-metallic solids: H₂O ice by Brown et al. [1], H₂O ice, and frozen gas of Xe, CO₂, and SF₆ by Bottiger et al. [2], ice of CO, Ar, and N₂, by Brown et al. [3], CO₂ ice by Mejia et al. [4], H₂O ice by Galli et al. [5], SiO₂, LiNbO₃, Al₂O₃, and Si₃N₄ by Qui et al. [6], UF₄ by Meins et al. [7], UO₂ by Bouffard et al. [8] and Schlutig [9], LiF and SiO₂ by Toulemonde et al. [10,11], SiO₂, SrTiO₃, SrCeO₃, CeO₂, MgO, TiO₂, and ZnO by Matsunami et al. [12], CaF₂, LaF₃, and UF₄ [11], NaCl, and RbI by Toulemonde et al. [13]. Also, it has been observed for Si₃N₄, AlN, Y₂O₃ and ZrO₂ [14], KBr and SiC [15], and Fe₂O₃ and TiN [16]. It is noticed that sputtering of frozen Xe films has been detected for low-energy electron impact, contrary to the anticipation of no atomic-displacement due to elastic collisions [2], confirming that electronic excitation plays an important role in sputtering. This paper concerns equilibrium charge incidence, which is achieved by the insertion of thin carbon and metal films. Sputtered atoms are collected in the catcher foils, and neutron activation methods for U detection [7–9] and ion beam analysis are utilized to obtain the sputtering yields.

The electronic energy deposition or electronic stopping power (S_e) of ions with equilibrium charge and the nuclear stopping power (S_n) can be calculated using TRIM or SRIM codes by Ziegler et al. [17,18]. Briefly, TRIM/SRIM codes utilize semi-empirical formulae derived from experimental data and dielectric response theory to calculate S_e for charged

particles and the interaction potential (the so-called ZBL potential) fitted to experimental data for S_n calculations. Characteristic features of electronic sputtering by high-energy ions [16] are reproduced:

- (a) Electronic sputtering yields per ion (Y_{SP}) superlinearly depend on S_e and are approximated by the power-law fit: $Y_{SP} = (B_{SP}S_e)^{N_{SP}}$ with $1 \leq N_{SP} \leq 4$ for most cases, B_{SP} being a material-dependent constant.
- (b) Y_{SP} is larger by $10\text{--}10^3$ than nuclear sputtering yields due to elastic collision cascades, which can be estimated assuming a linear dependence on S_n . The representative sputtering yields at $S_e = 10$ keV/nm by monatomic ions at normal incidence vary from 0.42 (MgO) [12] to 844 (WO₃) [16], and these yields are plotted as a function of the bandgap (E_g) and elastic constant. It appears that the sputtering yields tend to increase with the bandgap for $E_g > 3$ eV, and the yields decrease with the elastic constant for oxides. Stoichiometric sputtering has been observed for many materials, although only heavy elements such as U have been detected [7–9]. Non-stoichiometric sputtering has been argued for some fluorides (CaF₂, LaF₃ and UF₄) [11]. It should be mentioned that Bragg's additive rule is applied to obtain stopping powers for compound solids in the present study. The deviation from Bragg's rule is not serious for oxides and nitrides, being roughly 10% or less; around 1 MeV/u [16]. In most cases, the variation in S_e calculated using different versions of TRIM/SRIM is within 10% [16].

Furthermore, tracks (amorphous or disordered region along the ion trajectory for crystalline solids and density modification for amorphous solids) have been observed using transmission electron microscopy (TEM), Rutherford backscattering spectroscopy-channeling (RBS-C), small-angle X-ray scattering (SAXS), and atomic force microscopy (AFM). Here, some remarks for the results by monatomic ions are pointed out. Firstly, the S_e dependence of the track radius is much weaker than that of electronic sputtering. Secondly, tracks have been observed for S_e larger than the threshold (S_{eth}) in oxides (quartz or single-crystal SiO₂), mica, V₂O₅ glass, ZrSiO₄ (zircon), polyester resin, etc., (TEM) by Fleisher et al. [19] and summarized by Itoh et al. [20]. The threshold values scatter [20], and it seems that S_{eth} depends on the analysis methods.

Amorphization of SiO₂ quartz has been observed (RBS-C, TEM) by Meftah et al. [21], Toulemonde et al. [22], and (SAXS, TEM) Afra et al. [23]. At $S_e = 20$ keV/nm, the track radius reads 5.3 nm [21,22] and 3.8 nm (S_e averaged over the track length, S_e at the surface being 26 keV/nm (larger by 30% than the average)) [23]. Density modification, i.e., lower density in the track core surrounded by the shell with higher density, has been observed (SAXS) for amorphous (or vitreous) SiO₂, and the track radius is 5.4 nm (sum of core and shell radii) at $S_e = 16$ keV/nm (SAXS) by Kluth et al. [24]. The radius is somewhat larger than 4 nm in SiO₂ quartz [21,22]. Track radius (optical infrared spectroscopy (IR)) reads 6 nm at $S_e = 20$ keV/nm by Benyagoub et al. [25], a value comparable with the track radius in SiO₂ quartz. Toulemonde et al. have investigated track radius in amorphous SiO₂ for a wide range of S_e , and they have found no apparent threshold S_e of track formation due to synergy of the electronic and nuclear stopping powers [26]. For Al₂O₃ single crystal (sapphire), track radius (RBS-C) at $S_e = 30$ keV/nm reads 1.6 nm by Canut et al. [27], 1.7 nm by Khalifaoui et al. [28], and 2 nm of disordered region at $S_e = 25$ keV/nm (TEM analysis of strain) by O'Connell et al. [29]. Hillock radius reads 10 nm at $S_e = 30$ keV/nm (AFM), which is much larger than the track radius (the relationship between the hillock and track radii is not clear) [28].

Moreover, amorphization in a track for polycrystalline Si₃N₄ has been observed (TEM) by Zinkle et al. [30], and amorphization and density modification (TEM) by Vuuren et al. [31]. The track radius is 1.8 nm at $S_e \simeq 34$ keV/nm [30] and 1.9 nm at $S_e = 23$ keV/nm [31]. The track radius in the amorphized region is 3.1 nm ($S_e = 23$ keV/nm) [31]. Density modification similar to a-SiO₂ has been observed in a-SiN_{1.13} film (TEM) by Kitayama [32] and in a-SiN_{0.95}:H (SAXS) by Santiago [33]. The track radius is 5.5 nm ($S_e = 24$ keV/nm by 0.2 GeV Au ions) [32] and 4.1 nm ($S_e = 24$ keV/nm) [33]. The track radius in amorphous Si₃N₄ is larger than that in polycrystalline Si₃N₄. Disordered tracks have been observed in epilayer GaN by Kucheyev

et al. (TEM) [34] and Mansouri et al. (AFM) [35] and in epilayer GaN and InN by Sall et al. (TEM) [36]. The track radius is 5 nm ($S_e = 34$ keV/nm) [34], 1.5 nm ($S_e = 23\text{--}28$ keV/nm) [35], and 2.4 and 1.5 nm ($S_e = 46$ and 24 keV/nm, respectively) [36]. It is noticed that no track formation has been observed in AlN by monatomic ions up to $S_e = 33$ keV/nm, while it has been observed by irradiation of C cluster (fullerene) ions with $S_e > 20$ keV/nm. Cluster ion effects have not been understood yet. Disordered or amorphized regions have been observed in single-crystalline InP (RBS-C) by Kamarou et al. [37], and the track radius is 1.2–2.3 and 3 nm at $S_e = 19$ and 23 keV/nm, which are comparable with those in [36].

Comparison of electronic sputtering with lattice disordering (degradation of X-ray diffraction (XRD) intensity (Y_{XD})) has been reported for KBr and SiC [15] and SiO₂, ZnO, Fe₂O₃, TiN, and WO₃ [16]. As in the case of sputtering, it appears that Y_{XD} superlinearly depends on S_e , and the S_e dependence of Y_{XD} fits well to the power-law [15,16]. It would be worthwhile to extend investigations of lattice disordering to materials other than those mentioned above for a better understanding of electronic excitation effects. In this article, we have measured the lattice disordering of Cu₂O and Cu₃N films, and the results are compared with the sputtering results [38–40]. The results of high-energy ions (electronic excitation effects) will be compared with those of low-energy ions (elastic collision effects). The efficiency of the energy deposition on the material modification will be discussed.

2. Materials and Methods

XRD was measured using Cu- k_α radiation (typically, under X-ray operation conditions of 30 kV and 30 mA, with a scan step of 0.02° and a scan speed of several degrees per min). The XRD intensity was multiplied by the scan speed to obtain the ion fluence dependence. The accuracy of the XRD intensity was estimated to be approximately 10%, taking the variation of repeated measurements into account. RBS was performed with 1.8 MeV He ions at a scattering angle of 160° for evaluation of film thickness and composition. Similarly, the accuracy of the RBS was estimated considering the variation of repeated measurements. Ion irradiation was performed at room temperature and normal incidence. High-energy ion irradiation with lower incident charge than the equilibrium charge without a carbon foil is often employed for XRD measurement; however, the effect of non-equilibrium charge incidence does not come into play because the length for attaining the equilibrium charge is much smaller than the film thickness, as described later (after the description of sample preparation).

Cu₂O films were prepared on MgO substrate (thickness of 0.5 mm) at 700 °C using a reactive RF (radio frequency) magnetron sputtering (RFMS) method with a Cu disk target (purity of 99.99%) in Ar and O₂ gas [38,39]. According to XRD, the films are polycrystalline with diffraction peaks around 36°, with a very weak peak around 61° for unirradiated films [38,39]. These are assigned as (111) and (220) diffraction peaks of a cubic structure [41]. The peak of (111) diffraction is of concern in this study. The lattice parameter derived from the XRD result of unirradiated films is obtained to be 0.429 nm, which agrees well with the value of 0.427 nm in the literatures [41]. Film thickness is obtained to be ~100 and 76–99 nm for high- and low-energy ion irradiation, respectively. The composition is stoichiometric (the composition ratio of oxygen and copper, O/Cu = 0.5 ± 0.05). For the calculation of stopping powers, the film density is taken to be 6.0 gcm⁻³ (i.e., 5.0 × 10²² Cu cm⁻³) from the XRD results, which agrees with that in [42]. The attenuation length (L_{XA}) of Cu- k_α (8.0 keV) is obtained to be 36 μm [43], and the attenuation depth ($L_{XA} \sin(36^\circ/2)$) = 11 μm. The film thickness is much smaller than the attenuation depth, and thus, no correction is necessary for the XRD intensity.

Cu₃N films were prepared on R-cut-Al₂O₃ substrate (thickness of 0.3 mm) at 250 °C using a reactive RFMS deposition with a Cu disk of 99.99% in pure N₂ gas [40]. Diffraction peaks are observed at ~23° and 48° and assigned as (100) and (200) diffraction planes of a cubic structure [41]. The lattice parameter is obtained to be 0.3831 nm with a sample variation of 0.4% (20 samples) and is close to 0.3815 nm [41]. From the lattice parameter, the film density is estimated to be 5.4 × 10²² Cu cm⁻³ or 6.12 gcm⁻³ (close to 5.84 gcm⁻³ [42]), and this is employed for stopping power calculation. According to RBS of 1.8 MeV He, the film

thickness used in this study is 100–200 and 88 nm for high- and low-energy ion irradiation, respectively. The composition is evaluated to be roughly stoichiometric, considering poor accuracy (~30%) because of poor statistics of nitrogen yields. Similarly to Cu₂O, L_{XA} of Cu-k_α is obtained to be 34 μm [43], and the attenuation depth ($L_{XA} \sin(23^\circ/2)$) = 6.7 μm. The film thickness (90–200 nm) is much smaller than the attenuation depth, and thus, no correction is required for the XRD intensity.

The beam current density of 100 keV Ne⁺ and N⁺ ions has been 0.5–2 μAcm⁻² (flux of 0.3–1.3 × 10¹³ cm⁻²). The macroscopic temperature rise is estimated to be 40 °C [44]. The beam current of high-energy ions with the incident charge of +q has been ~1 particle nA (beam current divided by q or 6 × 10⁹ ions per cm⁻²), and an estimated temperature rise is 40 °C. This temperature rise is not significant for Cu₂O and will be discussed for Cu₃N in Section 3.3.

Following [45], the characteristic length (L_{EQ}) for attaining the equilibrium charge is estimated from the empirical formula of single-electron loss cross-section [46,47], with the first ionization potential (I_p) [42,48]; $L_{EQ} = 1/(\text{single-electron loss cross-section } (\sigma_{1L}) \text{ times } N)$, N being the atomic density. L_{EQ} and σ_{1L} are listed in Table 1. L_{EQ} is much smaller than the film thickness, and hence, the charge–state effect is insignificant in this study.

Table 1. Ion, energy (MeV), first ionization potential of ion (I_p , eV), effective number of removable electrons (N_{eff}), single-electron loss cross-section (σ_{1L} , 10⁻¹⁶ cm²), characteristic length (L_{EQ} , nm) attaining the equilibrium charge for Cu₂O and Cu₃N. I_p is taken from [42,48], and σ_{1L} is taken from [46,47].

Ion	E (MeV)	I_p (eV)	N_{eff}	σ_{1L} (10 ⁻¹⁶ cm ²)	L_{EQ} (Cu ₂ O) (nm)	L_{EQ} (Cu ₃ N) (nm)
⁵⁸ Ni ⁺¹⁰	90	321	8	0.358(Cu)	4.6	4.6
				0.152(O)		
				0.139(N)		
¹³⁶ Xe ⁺¹⁴	100	343	12	0.376(Cu)	4.4	4.4
				0.159(O)		
				0.146(N)		
¹³⁶ Xe ⁺¹⁴	200	343	12	0.392(Cu)	4.2	4.2
				0.166(O)		
				0.152(N)		

3. Results and Discussion

3.1. Cu₂O: High-Energy Ion Impact

XRD patterns of Cu₂O films are shown in Figures 1 and 2 for irradiation by 200 MeV Xe and 100 MeV Xe ions. It is seen that the XRD intensity decreases with the ion fluence, and the diffraction angle increases. The XRD intensity at a diffraction angle of ~36° (the most intensive (111) diffraction of cubic cuprite), normalized to that of unirradiated films (normalized intensity), is shown in Figure 3 as a function of ion fluence for 90 MeV Ni⁺¹⁰, 100 MeV Xe⁺¹⁴, and 200 MeV Xe⁺¹⁴ ions. It appears that the normalized XRD intensity is proportional to the ion fluence. From the slope, the XRD degradation yield per unit ion fluence (Y_{XD} , representing lattice disordering cross-section) is obtained, and the results are provided in Table 2. The linear relationship (Figure 3) can be understood by the idea that the normalized XRD intensity corresponds to $1 - \chi_{min}$. Here, χ_{min} is the minimum yield of RBS-C due to disordering or amorphization. A saturation formula [49] is often applied to the ion fluence dependence of χ_{min} : $\chi_{min} = 1 - \exp(-AF)$, A and F being the disordering cross-section and ion fluence, and χ_{mi} is proportional to F for low F . Lattice compaction has been observed, and the appreciable change begins at low fluence, as already reported [38]. The decrease in the lattice parameter per unit fluence (Y_{LC}) is obtained to be 2.5, 4.3, and 6.8×10^{-15} cm⁻² for 90 MeV Ni, 100 MeV Xe, and 200 MeV Xe ions, respectively, with an

estimated accuracy of 20%. S_e dependence of the lattice parameter change is fitted by a power-law and obtained to be $(0.123 \cdot S_e)^{1.54}$. It appears that the S_e dependence of Y_{LC} is weaker than that of Y_{XD} , as described later.

The electronic stopping power (S_e^*) appropriate for XRD intensity degradation is calculated using TRIM 1997 [17], with the approximation that the appropriate energy (E^*) is yielded by the energy at the middle of the film thickness (~ 50 nm), i.e., $S_e^* = S_e(E^*)$ with $E^* = E(\text{incidence}) - S_e(E) \cdot 50$ nm (Table 2). This correction is very close to that in C-foil, employed for sputtering measurements, and thus, the same S_e^* is adopted for both the XRD intensity degradation and sputtering (Table 2). Correction of S_e appears to be less than 1 percent. The areal density of Cu in the C-foil collector vs. ion fluence after revision [15] is shown in Figure 4. It is seen that Cu areal density is proportional to the ion fluence, and from the slope (Cu areal density/ion fluence), the sputtering yields of Cu (Y_{Cu}) are obtained. Here, the collection efficiency of Cu in the C-foil collector is taken to be 0.3 [38]. The total sputtering yields Y_{sp} of Cu_2O equal to 1.5 times Y_{Cu} , assuming stoichiometric sputtering. Y_{sp} of Cu_2O is summarized in Table 2. Comparison of S_e dependence of the disordering Y_{XD} with that of Y_{sp} is shown in Figure 5. Both Y_{XD} and Y_{sp} fit to the power-law. It is seen that Y_{XD} has a much stronger dependence than that of Y_{sp} and that of Y_{LC} , as mentioned above.

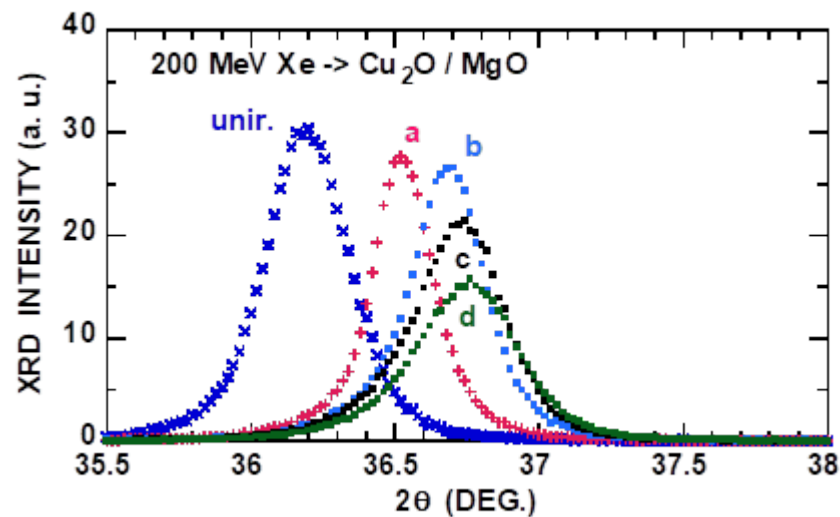


Figure 1. XRD patterns of (111) diffraction plane for unirradiated (x, blue) and irradiated Cu_2O films by 200 MeV Xe ions at 0.95 (a, red), 2.16 (b, light blue), 3.44 (c, black), and $7.15 \times 10^{12} \text{ cm}^{-2}$ (d, green).

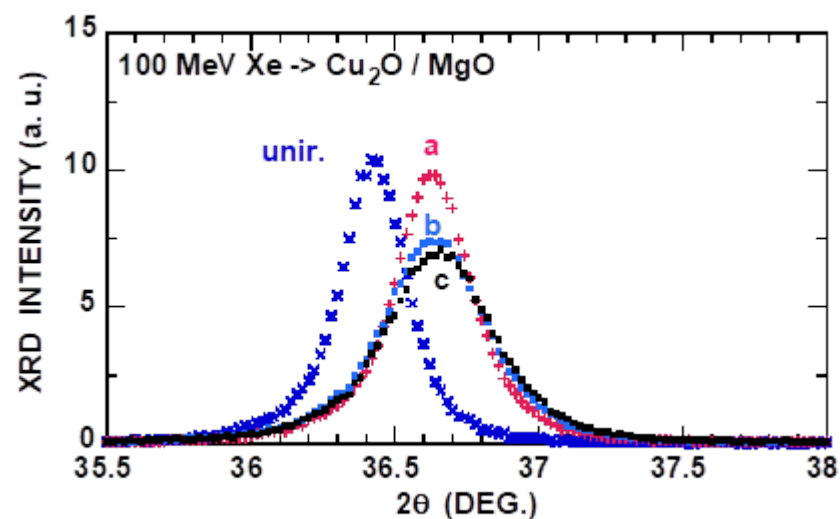


Figure 2. XRD patterns similar to Figure 1, except for 100 MeV Xe ions at 2.23 (a, red), 4.67 (b, light blue), and $6.67 \times 10^{12} \text{ cm}^{-2}$ (c, black).

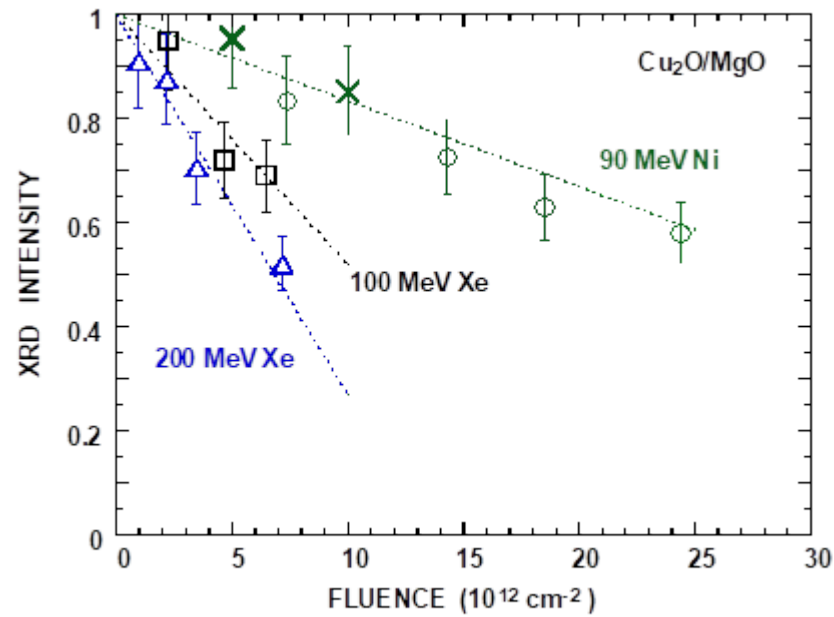


Figure 3. XRD intensity from (111) diffraction plane $36\text{--}37^\circ$, normalized to unirradiated films of Cu_2O as a function of ion fluence for 90 MeV Ni (o, x), 100 MeV Xe (\square), and 200 MeV Xe (Δ) ions. Data of 90 MeV Ni (x) from [38]. Linear fit is indicated by dotted lines. An estimated error of XRD intensity is 10%, as indicated by error bars.

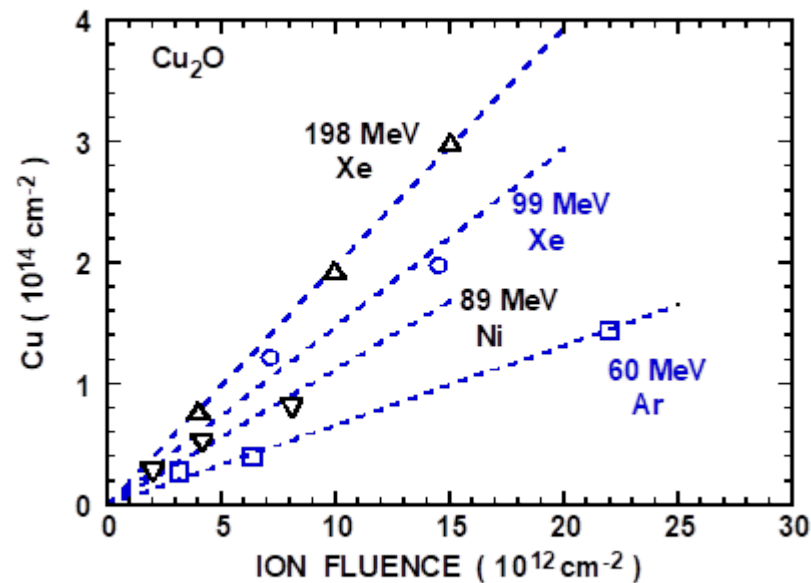


Figure 4. Areal density of sputtered Cu from Cu_2O on MgO substrate collected in carbon foil vs. ion fluence for 60 MeV Ar (\square), 89 MeV Ni (∇), 99 MeV Xe (o), and 198 MeV Xe (Δ) ions. An estimated error of areal density is 10%.

The optical absorption spectra of unirradiated Cu_2O and irradiated by 200 MeV Xe at $7.15 \times 10^{12} \text{ cm}^{-2}$ are shown in Figure 6. No appreciable change in optical absorption spectra by the ion irradiation is observed, as reported for 100 MeV Xe ions at $3 \times 10^{12} \text{ cm}^{-2}$ [38], except for a small reduction of a hump around the optical wavelength of $0.344 \mu\text{m}$. The bandgap (E_g) is obtained to be 2.54 and 2.52 eV for Cu_2O films of unirradiated and irradiated by 200 MeV Xe at $7.15 \times 10^{12} \text{ cm}^{-2}$ (Figure 7). Here, a relationship is employed: (absorbance \times photon energy)² is proportional to (photon energy $- E_g$). The present bandgap agrees well with 2.52 eV [50] and 2.51 eV after annealing [51], though a large scatter of the bandgap has been seen, (2–2.38 eV) pointed out in [39] and (2–2.6 eV) [50], and more com-

plications are discussed by Meyer et al. [52]. Aside from the determination of the bandgap, no appreciable change in the bandgap as well as optical absorption is observed for 200 MeV Xe at $7.15 \times 10^{12} \text{ cm}^{-2}$, 90 MeV Ni at $24 \times 10^{12} \text{ cm}^{-2}$, and 100 MeV Xe at $6 \times 10^{12} \text{ cm}^{-2}$, as reported for 100 MeV Xe at $3 \times 10^{12} \text{ cm}^{-2}$ [38]. The result of high-energy ion impact contrasts with that of low-energy ion impact, where E_g decreases with the ion fluence [39], and the difference of the high- and low-energy ion impact will be discussed in the next section. It would be worthwhile to mention that the optical absorbance ($OA = \text{Log}_{10}(I_0/I)$, I_0 and I being the incident and transmitted photon intensity) at 344 nm (3.6 eV) appears to be proportional to the film thickness L for unirradiated films. The absorbance coefficient (OA/L) is obtained to be 0.027 nm^{-1} after subtracting the OA of the MgO substrate (0.065), and the absorption coefficient α (defined by $I = I_0 \exp(-\alpha L)$) is $6.2 \times 10^5 \text{ cm}^{-1}$. The present absorption coefficient agrees with $6.77 \times 10^5 \text{ cm}^{-1}$ [53]. The OA coefficient is larger by a factor of ~ 4 than that of doped ZnO [54].

Table 2. XRD and sputtering data of Cu_2O films for high-energy ions. Ion, incident energy (E in MeV), XRD intensity degradation (Y_{XD}), sputtering yield (Y_{SP}), appropriate energy E^* (MeV) considering the energy loss in the film or carbon foil collector, electronic stopping power (S_e^*), nuclear stopping power (S_n^*) in keV/nm at E^* . The deviation $\Delta S_e^* = (S_e^*/S_e(E) - 1) \times 100$ is also provided. Stopping powers are calculated using TRIM1997. S_e^* calculated using SRIM2013 is provided in the parenthesis after S_e^* (TRIM1997).

Ion	E (MeV)	Y_{XD} (10^{-15} cm^2)	Y_{SP}	E^* (MeV)	S_e^* (keV/nm)	S_n^* (keV/nm)	ΔS_e^* (%)
^{136}Xe	200	73	98.8	198	27.55 (27.59)	0.115	-0.24
^{136}Xe	100	48	73.8	99	20.95 (21.61)	0.202	-0.62
^{58}Ni	90	16.5	56	89	15.12 (13.98)	0.0318	+0.026
^{40}Ar	60		33	60	8.52 (8.45)	0.014	0

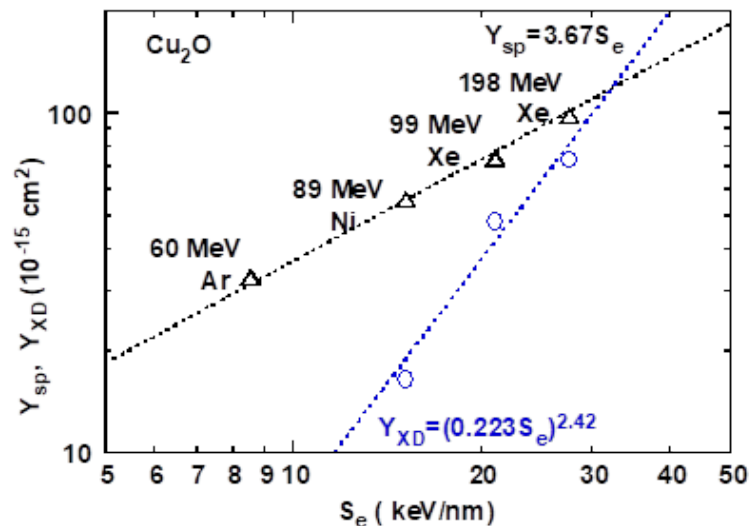


Figure 5. XRD intensity degradation Y_{XD} (10^{-15} cm^2) (o) and sputtering yield Y_{SP} (Δ) as a function of electronic stopping power, S_e (keV/nm). Also shown is power-law fit: $Y_{\text{XD}} = (0.223 S_e)^{2.42}$ and $Y_{\text{SP}} = 3.67 S_e$. An estimated error of Y_{XD} and Y_{SP} is 10%.

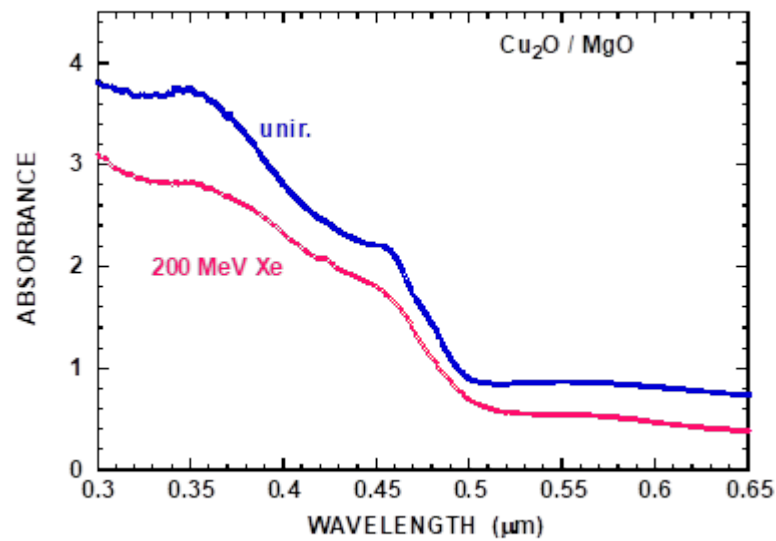


Figure 6. Optical absorption spectra of Cu_2O for unirradiated Cu_2O (blue) and Cu_2O irradiated by 200 MeV Xe at $7.2 \times 10^{12} \text{ cm}^{-2}$ (red).

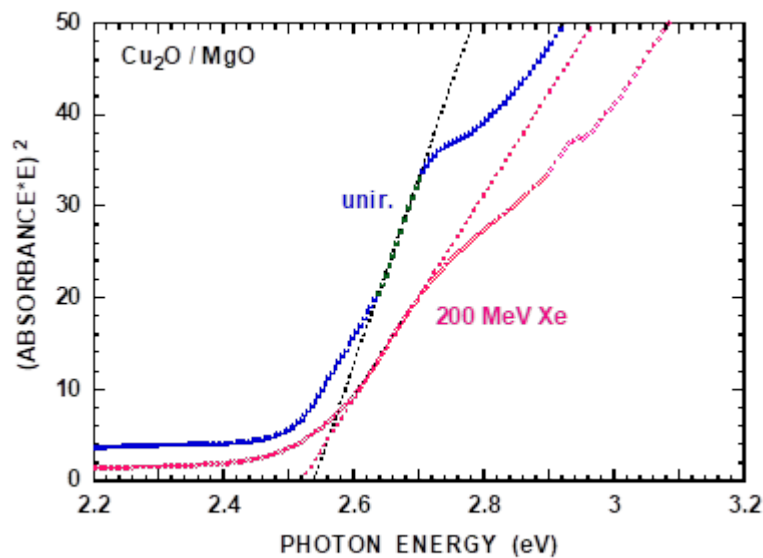


Figure 7. Square of optical absorbance times photon energy vs. photon energy of Cu_2O for unirradiated Cu_2O (blue) and Cu_2O irradiated by 200 MeV Xe at $7.2 \times 10^{12} \text{ cm}^{-2}$ (red), illustrating the bandgap.

3.2. Cu_2O : Low-Energy Ion Impact

XRD intensity at a diffraction angle of $\sim 36^\circ$, normalized to that of unirradiated films (normalized intensity), is shown in Figure 8 as a function of ion fluence for 100 keV N and 100 keV Ne. As in the case of high-energy ion impact (Figure 3), it is found that the normalized XRD intensity decreases proportionally to the ion fluence up to a certain fluence. The slope of the normalized intensity vs. ion fluence is reduced for high fluence, and this could be due to the overlapping effect. From the slope for low fluence, the XRD degradation yield per unit ion fluence (Y_{XD}), i.e., lattice disordering cross-section, is obtained, and the results are provided in Table 3. Lattice compaction is $\sim 2\%$ at $10 \times 10^{16} \text{ cm}^{-2}$ for both 100 keV N and Ne, nearly independent of the ion species. Ion, energy, film thickness, projected range (R_p), nuclear and electronic stopping powers averaged over the film thickness (L), and fraction retained of ions in the film (F_R) are summarized in Table 3, noting that for $L < R_p$, F_R may play roles in the modifications. Sputtering yields as well as the stopping powers at the surface are also provided in Table 3. The maximum fluence is 10 and $5.2 \times 10^{16} \text{ cm}^{-2}$ for sputtering measurements by 100 keV N and Ne ions, respectively. Averaged stopping powers differ from

those in [39], since the electronic energy loss carried by recoils is not taken into account in this study. This choice does not affect the following discussion.

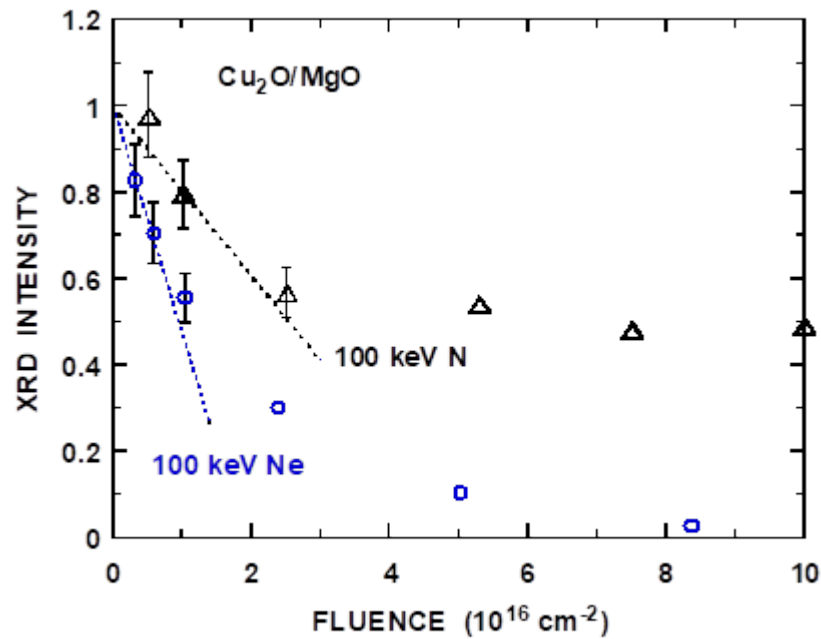


Figure 8. XRD intensity from (111) diffraction plane at $36\text{--}37^\circ$, normalized to unirradiated films of Cu_2O as a function of ion fluence for 100 keV N (Δ) and 100 keV Ne (\circ). Data of 100 keV Ne from [39]. Linear fit is indicated by dotted lines. An estimated error of XRD intensity is 10%, as indicated by error bars.

Table 3. XRD and sputtering data of Cu_2O films for low-energy ions. Ion, incident energy (E , keV), film thickness L (nm), projected range (R_p , nm), nuclear ($\langle S_n \rangle$) and electronic ($\langle S_e \rangle$) stopping powers averaged over film thickness relevant to XRD intensity degradation (Y_{XD} , $Y_{XD}(10^{-16} \text{ cm}^2)$), retained fraction of ions in film (F_R , %), nuclear (S_n) and electronic (S_e) stopping powers at surface relevant to sputtering, sputtering yield (Y_{SP}). Projected range, stopping powers, and retained fraction are calculated using TRIM1997. Sputtering data from [39].

Ion	E (keV)	L (nm)	R_p (nm)	$\langle S_n \rangle$ (keV/nm)	$\langle S_e \rangle$ (keV/nm)	Y_{XD} (10^{-16} cm^2)	F_R (%)	S_n (keV/nm)	S_e (keV/nm)	Y_{SP}
N	100	76	152	0.16	0.38	0.196	11	0.108	0.43	0.9
Ne	100	99	118	0.37	0.29	0.525	34	0.251	0.408	1.87

From Table 3, it is found that the ratio of Y_{XD} (100 keV Ne) over Y_{XD} (100 keV N) is obtained to be 2.68, and this ratio reasonably agrees with the ratio of the average nuclear stopping powers of 2.3. It is also found, as expected, that Y_{SP} (100 keV Ne)/ Y_{SP} (100 keV N) is obtained to be 2.08, in good agreement with the nuclear stopping power ratio of 2.3. Here, the so-called α -factor (order of unity, representing the efficiency of the nuclear stopping power contributing to nuclear sputtering [55]) is disregarded. Hence, lattice disordering and sputtering by low-energy ions are nearly proportional to the nuclear stopping power.

No appreciable change in E_g has been observed for high-energy ions. Thus, the observation that the ion fluence dependence of the decrease in the bandgap (E_g) is the same for 100 keV N and Ne ions cannot be explained by nuclear energy deposition or electronic energy deposition. This could be partly due to the implantation effect of low-energy ions, considering the appreciable retained fraction of 11% (100 keV N) and 34% (100 keV Ne), since it has been observed that XRD intensity variation in WNO_x films is identical for low-energy (~ 1 keV) H and D implantation [56]. However, it is not well understood yet at present why there is no ion species dependence of the bandgap decrease in Cu_2O with the ion fluence, and more investigations are desired.

3.3. Cu_3N

XRD patterns of Cu_3N films are shown in Figures 9 and 10 for irradiation by 200 MeV Xe and 100 MeV Xe ions. It is seen that the XRD intensity decreases with the ion fluence, and the diffraction angle remains unchanged. XRD intensity of Cu_3N films on R-cut Al_2O_3 at a diffraction angle of 23° (the most intensive (100) diffraction of cubic structure), normalized to that of unirradiated films (normalized intensity), is shown in Figure 11 as a function of ion fluence for 90 MeV Ni^{+10} , 100 MeV Xe^{+14} , and 200 MeV Xe^{+14} ions. It is reminded that the Cu phase has been observed at large fluence, meaning decomposition [40]. In this study, only low fluence is of concern, and it is assumed that decomposition does not play a significant role, and this point will be discussed later. It appears that the normalized XRD intensity is proportional to the ion fluence up to certain fluence. From the slope for low fluence, the XRD degradation yield per unit ion fluence (Y_{XD} , lattice disordering cross-section) is obtained, and the results are provided in Table 4. A small lattice compaction (-0.2% for 100 MeV Xe at 10^{13} cm^{-2} or $Y_{\text{LC}} \sim 2 \times 10^{-16} \text{ cm}^2$, which is much smaller than that for Cu_2O (Section 3.1)) or no appreciable change in the lattice parameter has been observed for the other high-energy ion impacts, including the results shown in Figures 9 and 10. Sputtering yields (Y_{sp}) by high-energy ions are also provided in Table 4. The maximum fluence for the sputtering measurement is $0.8, 2, 1.4,$ and $1.5 \times 10^{12} \text{ cm}^{-2}$ for 200 MeV Xe, 100 MeV Xe, 90 MeV Ni, and 60 MeV Ar ions. S_e dependence of Y_{XD} and Y_{sp} is shown in Figure 12.

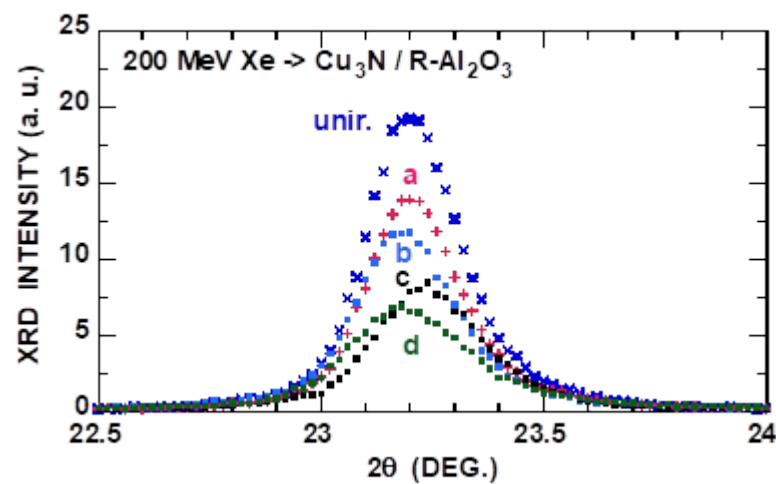


Figure 9. XRD patterns of (100) diffraction plane for unirradiated (blue) and irradiated Cu_3N films by 200 MeV Xe ions at 0.226 (a, red), 0.33 (b, light blue), 0.5 (c, black), and $1.02 \times 10^{12} \text{ cm}^{-2}$ (d, green).

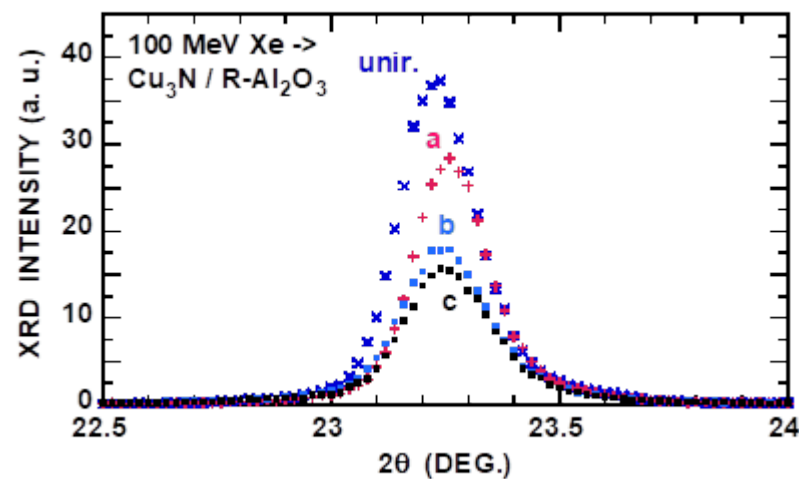


Figure 10. XRD patterns similar to Figure 9, except for 100 MeV Xe ions at 0.336 (a, red), 0.72 (b, light blue), and $0.98 \times 10^{12} \text{ cm}^{-2}$ (c, black).

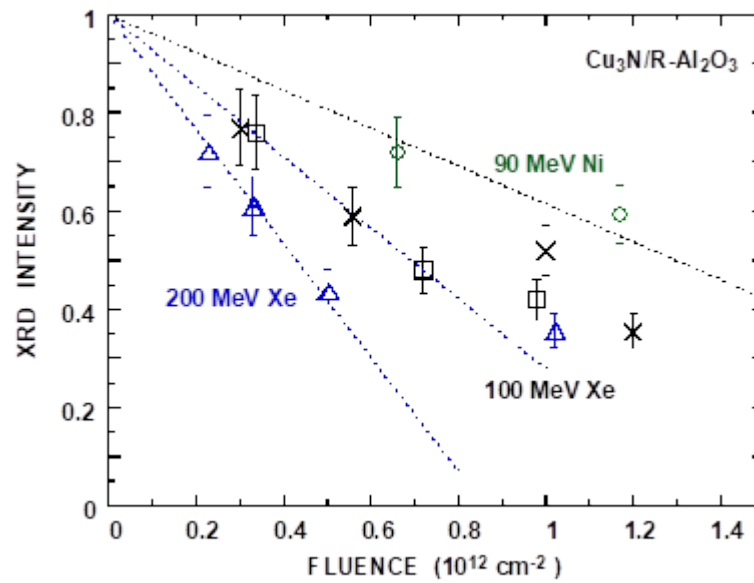


Figure 11. XRD intensity from (100) diffraction plane at nearly 23° , normalized to unirradiated films of Cu_3N as a function of ion fluence for 90 MeV Ni (o), 100 MeV Xe (\square , x), and 200 MeV Xe (Δ) ions. Data of 100 MeV Xe (x) from [40]. Linear fit is indicated by dotted lines. The estimated error of XRD intensity is 10%, as indicated by error bars.

Table 4. XRD and sputtering data of $\text{Cu}_3\text{N}/\text{R-Al}_2\text{O}_3$ films for high-energy ions. Ion, incident energy (E in MeV), XRD intensity degradation (Y_{XD}), sputtering yield (Y_{SP}), appropriate energy E^* (MeV) considering the energy loss in the film or carbon foil collector, electronic stopping power (S_e^*), nuclear stopping power (S_n^*) in keV/nm at E^* . The deviation $\Delta S_e^* = (S_e^*/S_e(E) - 1) \times 100$ is also provided. Stopping powers are calculated using TRIM1997. S_e^* calculated using SRIM2013 is provided in the parenthesis after S_e^* (TRIM1997).

Ion	E (MeV)	Y_{XD} (10^{-15} cm^2)	Y_{SP}	E^* (MeV)	S_e^* (keV/nm)	S_n^* (keV/nm)	ΔS_e^* (%)
^{136}Xe	200	116	960	198	27.37 (27.71)	0.116	-0.24
^{136}Xe	100	72	556	99	20.74 (21.64)	0.204	-0.62
^{58}Ni	90	38.5	342	89	15.03 (14.04)	0.0321	+0.02
^{40}Ar	60		142	60	8.47 (8.49)	0.0142	0

Normalized XRD intensity as a function of ion fluence for 100 keV N and 100 keV Ne ions is shown in Figure 13. The XRD degradation yield per unit ion fluence (Y_{XD}) is obtained, and the results are provided in Table 5. From Table 5, it is found that the ratio of Y_{XD} (100 keV Ne) over Y_{XD} (100 keV N) is obtained to be 2.45, and this ratio reasonably agrees with the average nuclear stopping power ratio of 2.2. Hence, the lattice disordering is nearly proportional to the nuclear stopping power. The Cu peak in the XRD appears at $0.82 \times 10^{15} \text{ cm}^{-2}$ ($\sim 1 \times 10^{15} \text{ cm}^{-2}$ [40]) for 100 keV Ne ion impact and $4.5 \times 10^{15} \text{ cm}^{-2}$ for 100 keV N ion impact, respectively. Lattice compaction is obtained to be 0.5% at $0.5 \times 10^{15} \text{ cm}^{-2}$ and 0.54% at $0.1 \times 10^{15} \text{ cm}^{-2}$ for 100 keV N and 100 keV Ne ions.

Sputtering yields of Cu_3N by 100 keV N and Ne ions are carefully reanalyzed, and the revised yields are obtained to be 3.2 and 7.6, respectively (Table 5). Here, the maximum ion fluence for the sputtering yield evaluation is 6 and $31 \times 10^{15} \text{ cm}^{-2}$ for 100 keV N and Ne, and the fluence is larger than that of the Cu phase appearance in the XRD patterns, as mentioned above. The sputtering yields are much larger than those of Cu_2O . The ratio, Y_{sp} (100 keV Ne)/ Y_{sp} (100 keV N), is obtained to be 2.38, and this agrees with the nuclear stopping power ratio of 2.22. Again, the so-called α -factor (order of unity, representing the efficiency of the nuclear stopping power contributing to nuclear sputtering [55]) is discarded. As

described in Section 2, the estimated macroscopic temperature rise is 40 °C [44]. This temperature rise is smaller than the thermal decomposition temperature, which ranges from 100 to 470 °C [57]. However, the possibility that the large sputtering yields are partly due to decomposition is not ruled out, even though the temperature rise is lower than the decomposition temperature.

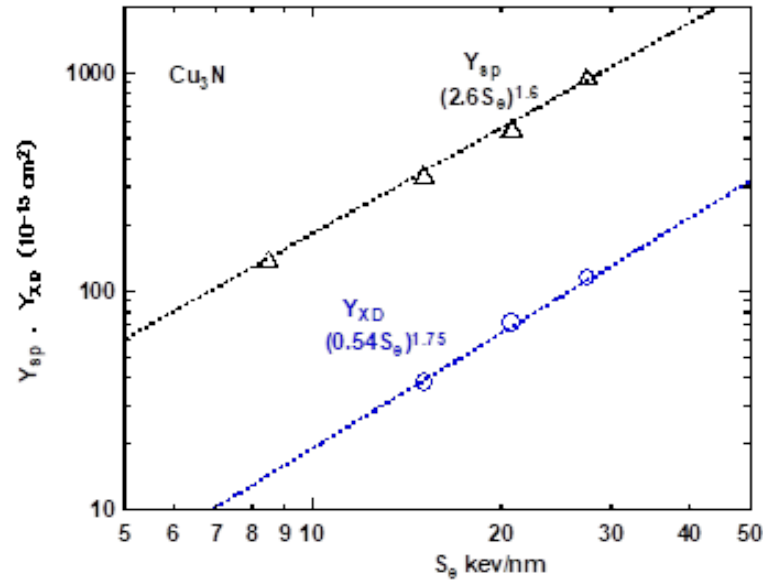


Figure 12. XRD intensity degradation Y_{XD} (10^{-15} cm 2) (o) and sputtering yield Y_{sp} (Δ) as a function of electronic stopping power, S_e (keV/nm). Also shown is power-law fit: Y_{XD} (10^{-15} cm 2) = $(0.54S_e)^{1.75}$ and $Y_{sp} = (2.6S_e)^{1.6}$. An estimated error of Y_{XD} and Y_{sp} is 10%.

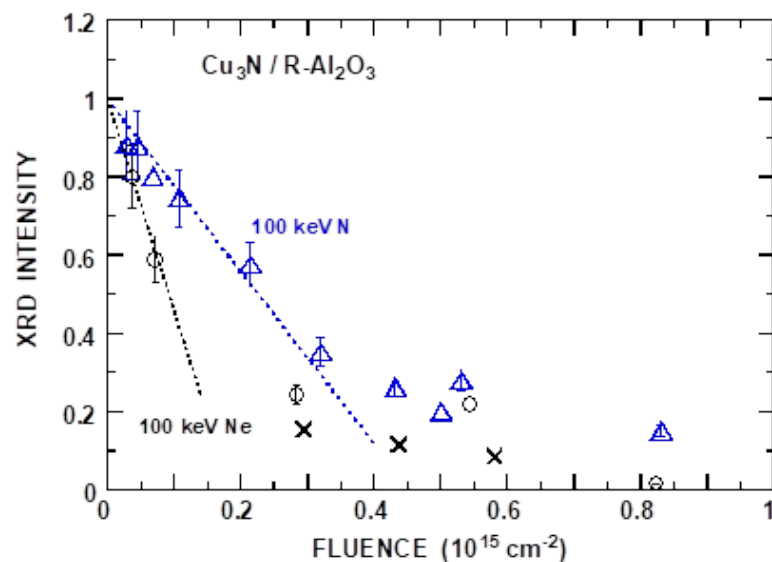


Figure 13. XRD intensity from (100) diffraction plane at nearly 23°, normalized to unirradiated films of Cu_3N as a function of ion fluence for 100 keV N (o) and 100 keV Ne (Δ , x) ions. Data of 100 keV Ne (x) from [40]. Linear fit is indicated by dotted lines. An estimated error of XRD intensity is 10%, as indicated by error bars.

The optical absorption spectra are shown in Figure 14 for unirradiated and irradiated Cu_3N films by 100 MeV Xe ions. Oscillations are seen in the unirradiated film, and these disappear upon ion irradiation, as in the case of 100 keV Ne impact [40]. The corresponding bandgap is obtained to be 1.38 and 1.22 eV, using the relation where the square root of the absorbance times the photon energy is proportional to the photon energy—bandgap

(Figure 15). The optical bandgap modification by ion impact is small. The absorbance of unirradiated films at $0.48 \mu\text{m}$ (photon energy of 2.58 eV), divided by the film thickness, is obtained to be 0.02 nm^{-1} after subtracting the OA of Al_2O_3 (0.065), and the absorption coefficient is found to be $4.6 \times 10^5 \text{ cm}^{-1}$, in reasonable agreement with $5.2 \times 10^5 \text{ cm}^{-1}$ [58].

Table 5. XRD and sputtering data of Cu_3N films for low-energy ions. Ion, incident energy (E , keV), film thickness L (nm), projected range (R_p nm), nuclear ($\langle S_n \rangle$) and electronic ($\langle S_e \rangle$) stopping powers (keV/nm) averaged over the film thickness relevant to XRD intensity degradation (Y_{XD}), Y_{XD} (10^{-15} cm^2), retained fraction of ions in film (F_R %), nuclear (S_n) and electronic (S_e) stopping powers at surface relevant to sputtering, sputtering yield (Y_{SP}). R_p , F_R , and stopping powers are calculated using TRIM1997.

Ion	E (keV)	L (nm)	R_p (nm)	$\langle S_n \rangle$ (keV/nm)	$\langle S_e \rangle$ (keV/nm)	Y_{XD} (10^{-15} cm^2)	F_R (%)	S_n (keV/nm)	S_e (keV/nm)	Y_{SP}
N	100	88	150	0.165	0.381	2.2	17	0.106	0.363	3.2
Ne	100	88	116	0.363	0.303	5.4	28	0.236	0.289	7.6

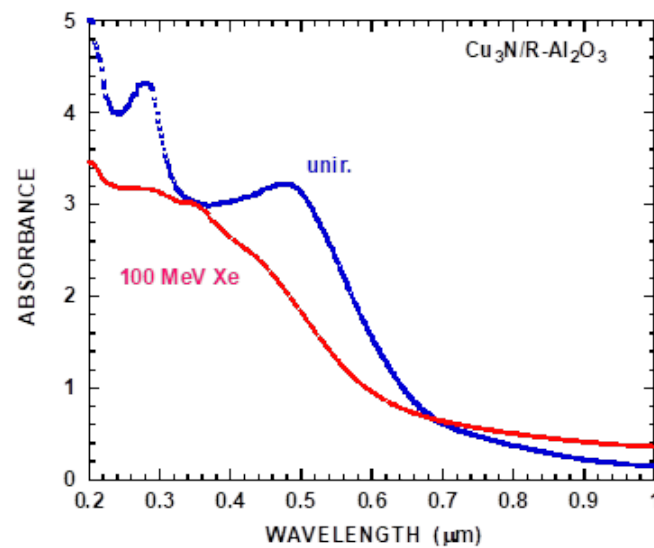


Figure 14. Optical absorption spectra of Cu_3N for unirradiated (blue) and irradiated Cu_3N by 100 MeV Xe at $1.2 \times 10^{12} \text{ cm}^{-2}$ (red).

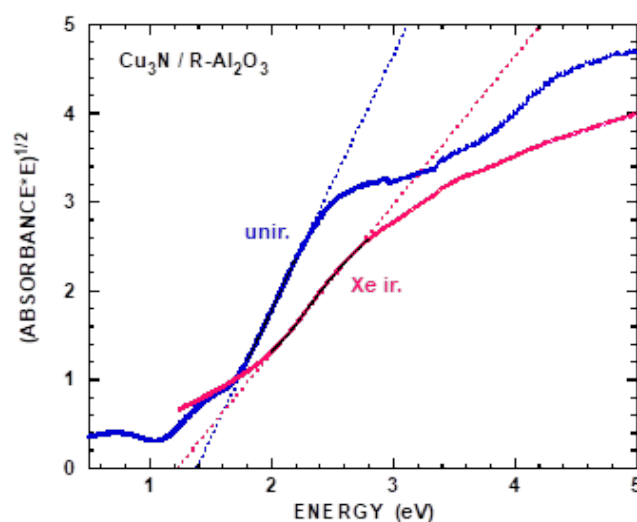


Figure 15. Square root of optical absorbance times photon energy vs. photon energy of Cu_3N for unirradiated Cu_3N (blue) and irradiated Cu_3N by 100 MeV Xe at $1.2 \times 10^{12} \text{ cm}^{-2}$ (red), illustrating the bandgap.

4. Discussion

The efficiency of electronic energy deposition is compared with that of nuclear energy deposition. Given the linear dependence of the electronic sputtering yield on S_e in the case of Cu_2O (Section 3.1), the effects of electronic and nuclear energy deposition on sputtering can be well defined for Cu_2O . The average of Y_{sp}/S_n (the effect of energy deposition) for two ion species is obtained as $7.9 \text{ (keV/nm)}^{-1}$ from Table 3, and this value is comparable with $3.67 \text{ (keV/nm)}^{-1}$ for electronic sputtering (Figure 3). The energy deposition efficiency is summarized in Table 6. Surprisingly, the results indicate that the energy deposition efficiency for sputtering is comparable within a factor of 2, irrespective of nuclear or electronic energy deposition, even though the effect of electronic energy deposition is an indirect process.

Table 6. A summary of the energy deposition efficiency. $R_{\text{XD}} = (Y_{\text{XD}}/S_e)/(Y_{\text{XD}}/S_n)$ and $R_{\text{sp}} = (Y_{\text{sp}}/S_e)/(Y_{\text{sp}}/S_n)$ are the efficiency ratios for lattice disordering and sputtering due to electronic and nuclear energy deposition. The values in the parenthesis are S_e (keV/nm), used for Y_{XD}/S_e evaluation.

Sample	Y_{XD}/S_e (10^{-16} cm^2) (keV/nm) $^{-1}$	Y_{XD}/S_n	R_{XD}	Y_{sp}/S_e	Y_{sp}/S_n	R_{sp}
Cu_2O	0.124 (15)	1.3	0.095	3.67	7.9	0.46
	0.256 (25)		0.20			
Cu_3N	26 (15)	140	0.19	23 (15)	31	0.7
	38 (25)		0.27	32 (25)		

Similarly, the average efficiency of nuclear energy deposition on lattice disordering of Cu_2O is obtained to be $1.3 \times 10^{-16} \text{ cm}^2 \text{ (keVnm)}^{-1}$ for low-energy ion impact from Table 3. For high-energy ion impact (Table 2 and Figure 5), a crude estimation of the efficiency of electronic energy deposition is obtained as $1.86 \times 10^{-16} \text{ cm}^2/15 \text{ keV/nm} = 0.124 \times 10^{-16} \text{ cm}^2 \text{ (keV/nm)}^{-1}$ at $S_e = 15 \text{ keV/nm}$. The efficiency is obtained as $0.256 \times 10^{-16} \text{ cm}^2 \text{ (keV/nm)}^{-1}$ at $S_e = 25 \text{ keV/nm}$. Hence, the effect of electronic energy deposition is much smaller than that of nuclear energy deposition (less efficient than electronic energy deposition). It might be surprising that for track formation in amorphous SiO_2 , the same effect of nuclear and electronic energy deposition has been argued [26], in contrast to the above results, noting that the track area and lattice disordering cross-section are similar for SiO_2 at high S_e [16].

For Cu_3N , the average energy deposition efficiency of sputtering for low-energy ions, Y_{sp}/S_n for two ion species, is obtained as 31 (keV/nm)^{-1} from Table 5, and this value is much larger than that of Cu_2O . Because of the super-linear dependence of electronic sputtering on S_e for high-energy ion impact on Cu_3N , a crude estimation is applied here, as mentioned above. The energy deposition efficiency, Y_{sp}/S_e for high-energy ions, is obtained as 23 and 32 (keV/nm)^{-1} at $S_e = 15$ and 25 keV/nm (Table 4 and Figure 12), and thus, the electronic energy deposition efficiency is comparable with the nuclear energy deposition efficiency for sputtering. The average energy deposition efficiency of lattice disordering for low-energy ions, Y_{XD}/S_n for two ion species, is obtained as $14 \times 10^{-15} \text{ cm}^2 \text{ (keV/nm)}^{-1}$ from Table 5, and this value is much larger than that of Cu_2O . The energy deposition efficiency, Y_{XD}/S_e for high-energy ions is obtained as 2.6 and $3.8 \times 10^{-15} \text{ cm}^2 \text{ (keV/nm)}^{-1}$ at $S_e = 15$ and 25 keV/nm (Table 4 and Figure 12), and thus, the electronic energy deposition efficiency is much smaller than the nuclear energy deposition efficiency for lattice disordering. The electronic and nuclear energy deposition efficiencies are comparable for sputtering, and the former is smaller (but less than an order of magnitude) than the latter for lattice disordering.

5. Conclusions

We have measured lattice disordering in polycrystalline Cu_2O and Cu_3N films using high- and low-energy ions. We find that lattice disordering is caused by electronic excitation

for high-energy ion impacts, and the degradation of XRD intensity (lattice disordering cross-section) fits a power-law relationship with electronic stopping power. The degradation of XRD intensity by low-energy ion impact (elastic collisions dominate) is found to be nearly proportional to the nuclear stopping power. We have discussed the efficiency of electronic and nuclear energy deposition on lattice disordering as well as sputtering. It appears that the efficiency of electronic and nuclear energy deposition is comparable for the sputtering of Cu_2O and Cu_3N . In the case of lattice disordering of Cu_2O and Cu_3N , we find that the electronic energy deposition efficiency is smaller than the nuclear energy deposition efficiency.

Author Contributions: Conceptualization and writing, N.M.; investigation, M.S., S.O. and B.T. All authors have read and agreed to the published version of the manuscript.

Funding: This research received no external funding.

Institutional Review Board Statement: Not applicable.

Informed Consent Statement: Not applicable.

Data Availability Statement: Data are contained within the article.

Acknowledgments: XRD has been measured using RIGAKU ULTIMA IV and RAD IIc at Radioisotope Research Center, Nagoya University. Rutherford backscattering spectroscopy and low-energy ion irradiation were performed using AN Van de Graaff and 200 kV ion accelerators, respectively, at Nagoya University. High-energy ion irradiation was done using a TANDEM accelerator at Tokai Research Center, JAEA.

Conflicts of Interest: The authors declare no conflicts of interest.

References

1. Brown, W.L.; Augustyniak, W.M.; Brody, E.; Cooper, B.; Lanzerotti, L.J.; Ramirez, A.; Evatt, R.; Johnson, R.E. Energy Dependence of the Erosion of H_2O Ice Films by H and He Ions. *Nucl. Instrum. Methods* **1980**, *170*, 321–325. [[CrossRef](#)]
2. Bottiger, J.; Davies, J.A.; L'Ecuyer, J.; Matsunami, N.; Ollerhead, R. Erosion of Frozen-Gas Films by MeV Ions. *Radiat. Eff.* **1980**, *49*, 119–124. [[CrossRef](#)]
3. Brown, W.L.; Lanzerotti, L.J.; Marcantonio, K.J.; Johnson, R.E.; Reimann, C.T. Sputtering of Ices by High Energy Particle Impact. *Nucl. Instrum. Methods B* **1986**, *14*, 392–402. [[CrossRef](#)]
4. Mejia, C.; Bender, M.; Severin, D.; Trautmann, C.; Boduch, P.; Bordalo, V.; Domaracka, A.; Lv, X.Y.; Martinez, R.; Rothard, H. Radiolysis and sputtering of carbon dioxide ice induced by swift Ti, Ni and Xe ions. *Nucl. Instrum. Methods B* **2015**, *365*, 477–481. [[CrossRef](#)]
5. Galli, A.; Vorburger, A.; Wurz, P.; Tulej, M. Sputtering of water ice films: A re-assessment with singly and doubly charged oxygen and argon ions, molecular oxygen, and electrons. *Icarus* **2017**, *291*, 36–45. [[CrossRef](#)]
6. Qiu, Y.; Griffith, J.E.; Meng, W.J.; Tombrello, T.A. Sputtering of Silicon and its Compounds in the Electronic Stopping Region. *Radiat. Eff.* **1983**, *70*, 231–236. [[CrossRef](#)]
7. Meins, C.K.; Griffith, J.E.; Qiu, Y.; Mendenhall, M.H.; Seiberling, L.E.; Tombrello, T.A. Sputtering of UF_4 by High Energy Heavy Ions. *Radiat. Eff.* **1983**, *71*, 13–33. [[CrossRef](#)]
8. Bouffard, S.; Duraud, J.P.; Mosbah, M.; Schlutig, S. Angular distribution of the sputtered atoms from UO_2 under high electronic stopping power irradiation. *Nucl. Instrum. Methods B* **1998**, *141*, 372–377. [[CrossRef](#)]
9. Schlutig, S. Contribution a L'etude de la Pulverisation et de L'endommagement du Dioxyde D'uranium par les Ions Lourds Rapides. Ph.D. Thesis, University of CAEN, Caen, France, 2001.
10. Toulemonde, M.; Assmann, W.; Trautmann, C.; Gruner, F. Jetlike Component in Sputtering of LiF Induced by Swift Heavy Ions. *Phys. Rev. Lett.* **2002**, *88*, 057602. [[CrossRef](#)]
11. Toulemonde, M.; Assmann, W.; Muller, D.; Trautmann, C. Electronic sputtering of LiF, CaF_2 , LaF_3 and UF_4 with 197 MeV Au ions: Is the stoichiometry of atom emission preserved? *Nucl. Instrum. Methods B* **2017**, *406*, 501–507. [[CrossRef](#)]
12. Matsunami, N.; Sataka, M.; Iwase, A.; Okayasu, S. Electronic excitation induced sputtering of insulating and semiconducting oxides by high energy heavy ions. *Nucl. Instrum. Methods B* **2003**, *209*, 288–293. [[CrossRef](#)]
13. Toulemonde, M.; Assmann, W.; B.-d'Etat, B.; Bender, M.; Bergmaier, A.; Boduch, P.; Negra, S.D.; Duan, J.; E.-Said, A.S.; Gruner, F.; et al. Sputtering of LiF and other halide crystals in the electronic energy loss regime. *Eur. Phys. J. D* **2020**, *74*, 144. [[CrossRef](#)]
14. Matsunami, N.; Sataka, M.; Okayasu, S.; Tazawa, M. Electronic sputtering of nitrides by high-energy ions. *Nucl. Instrum. Methods B* **2007**, *256*, 333–336. [[CrossRef](#)]
15. Matsunami, N.; Okayasu, S.; Sataka, M.; Tsuchiya, B. Electronic sputtering of SiC and KBr by high energy ions. *Nucl. Instrum. Methods B* **2020**, *478*, 80–84. [[CrossRef](#)]

16. Matsunami, N.; Sataka, M.; Okayasu, S.; Tsuchiya, B. Modification of SiO₂, ZnO, Fe₂O₃ and TiN Films by Electronic Excitation under High Energy Ion Impact. *Quantum Beam Sci.* **2021**, *5*, 30. [[CrossRef](#)]
17. Ziegler, J.F.; Biersack, J.P.; Littmark, U. *The Stopping and Range of Ions in Solids*; Pergamon Press: New York, NY, USA, 1985; pp. 1–321.
18. Ziegler, J.F.; Ziegler, M.D.; Biersack, J.P. SRIM-The stopping and range of ions in matter (2010). *Nucl. Instrum. Methods B* **2010**, *268*, 1818–1823. [[CrossRef](#)]
19. Fleischer, R.L.; Price, P.B.; Walker, R.M. Ion Explosion Spike Mechanism for Formation of Charged-Particle Tracks in Solids. *J. Appl. Phys.* **1965**, *36*, 3645–3652. [[CrossRef](#)]
20. Itoh, N.; Duffy, D.M.; Khakshouri, S.; Stoneham, A.M. Making tracks: Electronic excitation roles in forming swift heavy ion tracks. *J. Phys. Condens. Matter* **2009**, *21*, 474205. [[CrossRef](#)]
21. Meftah, A.; Brisard, F.; Costantini, J.M.; Dooryhee, E.; H.-Ali, M.; Hervieu, M.; Stoquert, J.P.; Studer, F.; Toulemonde, M. Track formation in SiO₂ quartz and the thermal-spike mechanism. *Phys. Rev. B* **1994**, *49*, 12457–12463. [[CrossRef](#)]
22. Toulemonde, M.; Bouffard, S.; Studer, F. Swift heavy ions in insulating and conducting oxides: Tracks and physical properties. *Nucl. Instrum. Methods B* **1994**, *91*, 108–123. [[CrossRef](#)]
23. Afra, B.; Rodriguez, M.D.; Trautmann, C.; Pakarinen, O.H.; Djurabekova, F.; Nordlund, K.; Bierschenk, T.; Giuliani, R.; Ridgway, M.C.; Rizza, G. SAXS investigation of the morphology of swift heavy ion tracks in α -quartz. *J. Phys. Condens. Matter.* **2013**, *25*, 045006. [[CrossRef](#)]
24. Kluth, P.; Pakarinen, O.H.; Djurabekova, F.; Giuliani, R.; Ridgway, M.C.; Byrne, A.P.; Nordlund, K. Nanoscale density fluctuations in swift heavy ion irradiated amorphous SiO₂. *J. Appl. Phys.* **2011**, *110*, 123520. [[CrossRef](#)]
25. Benyagoub, A.; Toulemonde, M. Ion tracks in amorphous silica. *J. Mater. Res.* **2015**, *30*, 1529–1543. [[CrossRef](#)]
26. Toulemonde, M.; Weber, W.J.; Li, G.; Shutthanandan, V.; Kluth, P.; Yang, T.; Wang, Y.; Zhang, Y. Synergy of nuclear and electronic energy losses in ion-irradiation processes: The case of vitreous silicon dioxide. *Phys. Rev. B* **2011**, *83*, 054106. [[CrossRef](#)]
27. Canut, B.; Benyagoub, A.; Marest, G.; Meftah, A.; Moncoffre, N.; Ramos, S.M.M.; Studer, F.; Thevenard, P.; Toulemonde, M. Swift-uranium-ion-induced damage in sapphire. *Phys. Rev. B* **1995**, *51*, 12194–12201. [[CrossRef](#)]
28. Khalfaoui, N.; Stoquert, J.P.; Haas, F.; Trautmann, C.; Meftah, A.; Toulemonde, M. Damage creation threshold of Al₂O₃ under swift heavy ion irradiation. *Nucl. Instrum. Methods B* **2012**, *286*, 247–253. [[CrossRef](#)]
29. O’Connell, J.H.; Rymzhanov, R.A.; Skuratov, V.A.; Volkov, A.E.; Kirilkin, N.S. Latent tracks and associated strain in Al₂O₃ irradiated with swift heavy ions. *Nucl. Instrum. Methods B* **2016**, *374*, 97–101. [[CrossRef](#)]
30. Zinkle, S.J.; Skuratov, V.A.; Hoelzer, D.T. On the conflicting roles of ionizing radiation in ceramics. *Nucl. Instrum. Methods B* **2002**, *191*, 758–766. [[CrossRef](#)]
31. van Vuuren, A.J.; Ibrayeva, A.D.; Skuratov, V.A.; Zdorovets, M.V. Analysis of the microstructural evolution of silicon nitride irradiated with swift Xe ions. *Ceram. Int.* **2020**, *46*, 7155–7160. [[CrossRef](#)]
32. Kitayama, T.; Morita, Y.; Nakajima, K.; Narumi, K.; Saitoh, Y.; Matsuda, M.; Sataka, M.; Tsujimoto, M.; Isoda, S.; Toulemonde, M.; et al. Formation of ion tracks in amorphous silicon nitride films with MeV C₆₀ ions. *Nucl. Instrum. Methods B* **2015**, *356–357*, 22–27. [[CrossRef](#)]
33. Mota-Santiago, P.; Vazquez, H.; Bierschenk, T.; Kremer, F.; Nadzri, A.; Schauries, D.; Djurabekova, F.; Nordlund, K.; Trautmann, C.; Mudie, S.; et al. Nanoscale density variations induced by high energy heavy ions in amorphous silicon nitride and silicon dioxide. *Nanotechnology* **2018**, *29*, 144004. [[CrossRef](#)] [[PubMed](#)]
34. Kucheyev, S.O.; Timmers, H.; Zou, J.; Williams, J.S.; Jagadish, C.; Li, G. Lattice damage produced in GaN by swift heavy ions. *J. Appl. Phys.* **2004**, *95*, 5360–5365. [[CrossRef](#)]
35. Mansouri, S.; Marie, P.; Dufour, C.; Nouet, G.; Monnet, I.; Lebius, H.; Benamara, Z.; Al-Douri, Y. Swift heavy ion effects in gallium nitride. *Int. J. Nanoelectron. Mater.* **2008**, *1*, 101–106.
36. Sall, M.; Monnet, I.; Moisy, F.; Grygiel, C.; J.-Leclerc, S.; Della-Negra, S.; Toulemonde, M.; Balanzat, E. Track formation in III-N semiconductors irradiated by swift heavy ions and fullerene and re-evaluation of the inelastic thermal spike model. *J. Mater. Sci.* **2015**, *50*, 5214–5227. [[CrossRef](#)]
37. Kamarou, A.; Wesch, W.; Wandler, E.; Undisz, A.; Rettenmayr, M. Swift heavy ion irradiation of InP: Thermal spike modeling of track formation. *Phys. Rev. B* **2006**, *73*, 184107. [[CrossRef](#)]
38. Matsunami, N.; Sataka, M.; Okayasu, S.; Ishikawa, N.; Tazawa, M.; Kakiuchida, H. High-energy ion irradiation effects on atomic structures and optical properties of copper oxide and electronic sputtering. *Nucl. Instrum. Methods B* **2008**, *266*, 2986–2989. [[CrossRef](#)]
39. Matsunami, N.; Fukuoka, O.; Tazawa, M.; Kakiuchida, H.; Sataka, M. Electronic structure modifications of cuprous-oxide films by ions. *Surf. Coat. Technol.* **2009**, *203*, 2642–2645. [[CrossRef](#)]
40. Matsunami, N.; Kakiuchida, H.; Tazawa, M.; Sataka, M.; Sugai, H.; Okayasu, S. Electronic and atomic structure modifications of copper nitride films by ion impact and phase separation. *Nucl. Instrum. Methods B* **2009**, *267*, 2653–2656. [[CrossRef](#)]
41. Joint Committee on Powder Diffraction Standards (JCPDS) 50667 (Cu₂O) and 21156 (Cu₃N).
42. Lide, D.R. (Ed.) *CRC Handbook of Chemistry and Physics*, 84th ed.; CRC Press: Boca Raton, FL, USA, 2003.
43. Storm, E.; Israel, H.I. Photon Cross Sections from 1 keV to 100 MeV for Elements Z = 1 to Z = 100. *Nucl. Data Tables A* **1970**, *7*, 565–681. [[CrossRef](#)]

44. Matsunami, N.; Yajima, T.; Iwahara, H. Permeation of implanted deuterium through SrCeO₃ (5% Yb). *Nucl. Instrum. Methods B* **1992**, *65*, 278–281. [[CrossRef](#)]
45. Matsunami, N.; Sataka, M.; Okayasu, S.; Tsuchiya, B. Charge State Effect of High Energy Ions on Material Modification in the Electronic Stopping Region. *Atoms* **2021**, *9*, 36. [[CrossRef](#)]
46. DuBois, R.D.; Santos, A.C.F.; Olson, R.E. Scaling laws for electron loss from ion beams. *Nucl. Instrum. Methods A* **2005**, *544*, 497–501. [[CrossRef](#)]
47. DuBois, R.D.; Santos, A.C.F. Target-Scaling Properties for Electron Loss by Fast Heavy Ions. In *Atomic Processes in Basic and Applied Physics*; Shevelko, V., Tawara, H., Eds.; Springer: Berlin/Heidelberg, Germany, 2012; Chapter 8; pp. 185–209.
48. Rodrigues, G.C.; Indelicato, P.; Santos, J.P.; Patte, P.; Parente, F. Systematic calculation of total atomic energies of ground state configurations. *At. Data Nucl. Data Tables* **2004**, *86*, 117–233. [[CrossRef](#)]
49. Weber, W.J. Models and mechanisms of irradiation-induced amorphization in ceramics. *Nucl. Instrum. Methods B* **2000**, *166–167*, 98–106. [[CrossRef](#)]
50. Chen, A.; Long, H.; Li, X.; Li, Y.; Yang, G.; Lu, P. Controlled growth and characteristics of single-phase Cu₂O and CuO films by pulsed laser deposition. *Vacuum* **2009**, *83*, 927–930. [[CrossRef](#)]
51. Wang, Y.; Miska, P.; Pilloud, D.; Horwat, D.; Mucklich, F.; Pierson, J.F. Transmittance enhancement and optical band gap widening of Cu₂O thin films after air annealing. *J. Appl. Phys.* **2014**, *115*, 073505. [[CrossRef](#)]
52. Meyer, B.K.; Polity, A.; Reppin, D.; Becker, M.; Hering, P.; Klar, P.J.; Sander, T.; Reindl, C.; Benz, J.; Eickhoff, M.; et al. Binary copper oxide semiconductors: From materials towards devices. *Phys. Status Solidi B* **2012**, *249*, 1487–1509. [[CrossRef](#)]
53. Malerba, C.; Biccari, F.; Ricardo, C.L.A.; D’Incau, M.; Scardi, P.; Mittiga, A. Absorption coefficient of bulk and thin film Cu₂O. *Sol. Energy Mater. Sol. Cells* **2011**, *95*, 2848–2854. [[CrossRef](#)]
54. Matsunami, N.; Itoh, M.; Kato, M.; Okayasu, S.; Sataka, M.; Kakiuchida, H. Ion induced modifications of Mn-doped ZnO films. *Nucl. Instrum. Methods B* **2015**, *365*, 191–195. [[CrossRef](#)]
55. Matsunami, N.; Yamamura, Y.; Itikawa, Y.; Itoh, N.; Kazumata, Y.; Miyagawa, S.; Morita, K.; Shimizu, R.; Tawara, H. Energy Dependence of the Ion-Induced Sputtering Yields of Monatomic Solids. *Atom. Data Nucl. Data Tables* **1984**, *31*, 1–80. [[CrossRef](#)]
56. Matsunami, N.; Ohno, N.; Tokitani, M.; Tsuchiya, B.; Sataka, M.; Okayasu, S. Modifications of WNO_x films by keV D and H ions. *Surf. Coat. Technol.* **2020**, *394*, 125798. [[CrossRef](#)]
57. Pierson, J.F. Structure and properties of copper nitride films formed by reactive magnetron sputtering. *Vacuum* **2002**, *66*, 59–64. [[CrossRef](#)]
58. Borsa, D.M.; Boerma, D.O. Growth, structural and optical properties of Cu₃N films. *Surf. Sci.* **2004**, *548*, 95–105. [[CrossRef](#)]

Disclaimer/Publisher’s Note: The statements, opinions and data contained in all publications are solely those of the individual author(s) and contributor(s) and not of MDPI and/or the editor(s). MDPI and/or the editor(s) disclaim responsibility for any injury to people or property resulting from any ideas, methods, instructions or products referred to in the content.